EVALUATION OF DIFFERENT CALIBRATION APPROACHES FOR S-NPP CRIS FULL SPECTRAL RESOLUTION SDR PROCESSING

Yong Chen[1], Yong Han[2]

[1]Earth System Science Interdisciplinary Center, University of Maryland, College Park, MD, USA
[2]NOAA Center for Satellite Applications and Research, College Park, MD, USA

ABSTRACT

The Cross-track Infrared Sounder (CrIS) on Suomi National Polar-orbiting Partnership Satellite (S-NPP) is a Fourier transform spectrometer and provides a total of 1305 and 2211 channels in normal spectral resolution (NSR) mode and full spectral resolution (FSR) mode, respectively, for sounding the atmosphere. NOAA operated CrIS in FSR mode on December 4, 2014 for S-NPP, and will operate CrIS in FSR mode for the Joint Polar Satellite System (JPSS). Based on CrIS Algorithm Development Library (ADL), CrIS full resolution processing system (CRPS) has been developed to generate the FSR Sensor Data Record (SDR). This code can also be run for normal mode and truncation mode SDRs. In order to select the best calibration algorithm for JPSS-1, four different calibration approaches are being implemented in the ADL full resolution code. In this study, evaluation results from different calibration approaches are presented and the ringing features observed in CrIS unapodized spectra are discussed.

***Index Terms*—** CrIS, calibration approaches, full spectral resolution (FSR), ringing artifact, S-NPP, JPSS

1. INTRODUCTION

CrIS is a Fourier transform spectrometer on S-NPP, which was launched on 28 October 2011. CrIS provides double-sided interferogram measurements. One typical CrIS scan sequence consists of 34 interferometer sweeps that comprise 30 fields-of-regard (FORs), or Earth scenes, plus 2 Deep Space (DS) and 2 Internal Calibration Target (ICT) measurements (these numbers include both moving mirror forward and reverse sweeps). Each FOR includes nine fields-of-view (FOVs). At each FOV, CrIS measures the infrared radiance covering three spectral bands. It provides a total of 1305 channels in the NSR operational mode for sounding the atmosphere. CrIS can also be operated in the FSR mode, in which the mid-wave (MWIR) and short-wave (SWIR) band interferograms are recorded with the same maximum path difference as the long-wave (LWIR) band and with spectral resolution of 0.625 cm^{-1} for all three bands (total 2211 channels) (NSR resolutions are 0.625, 1.25, 2.5 cm^{-1} for LWIR, MWIR, and SWIR, respectively).

The FSR mode was commanded on December 4, 2014. After the transition of the CrIS instrument from the NSR to FSR mode operation, the operational processing software Interface Data Processing Segment (IDPS) continued to process the Raw Data Records (RDRs) into NSR SDRs by truncating the MWIR and SWIR band data into the NSR interferograms. In order to provide FSR SDR data to the user community, an ADL based FSR processing system CRPS was developed to transform the RDRs into FSR SDRs [1]. CrIS SDR product comprises the radiance, noise (NEdN), geolocation, and data quality [2]. The FSR SDRs data are available to the public via the NOAA Center for Satellite Application and Research (STAR) FTP site: ftp://ftp2.star.nesdis.noaa.gov/smcd/xxiong/. Note that the CrIS SDR radiance spectra are unapodized.

The Earth scene (ES) view measurements are calibrated radiometrically [3] and spectrally [4] with two known targets: the near blackbody Internal Calibration Target and the Deep Space view whose radiance is negligible in the frequency range of CrIS measurements. The current calibration approach does the radiometric calibration first, and then applies the correction matrix operator (CMO) for spectral calibration, which includes the post calibration filter (f_{ATBD}), spectral resampling (F), self-apodization (SA) removal and residual (R) instrument line shape (ILS) removal. The ringing artifacts, which are defined as spectral features with the form of every other channel jumping up and down, are observed in CrIS normal mode SDR un-apodized spectra for this operational calibration approach [5]. The ringing artifacts are also depending on Optical Path Difference (OPD) sweep direction.

In this study, four different calibration approaches [6, 7] are implemented in the FSR ADL code to study and understand the ringing artifacts and to support to select the best calibration algorithm for CrIS on JPSS-1 [8].

2. CALIBRATION APPROACHES

Four calibration approaches based on the recommendation from the CrIS science team are implemented in the CRPS.

These calibration approaches can be divided into two categories based on the calibration order: radiometric calibration first, then CMO to spectral calibration; CMO to spectral first, then radiometric calibration.

TABLE 1
DIFFERENT RESAMPLING MATRIX FORMS

Bin Size N	Resampling Matrix (F)
Small N, (N): Number of bins after decimation	$F[k,k'] = \frac{\Delta\sigma_s}{\Delta\sigma_u} \frac{Sin(\pi \frac{\sigma_{s,k'} - \sigma_{u,k}}{\Delta\sigma_u})}{NSin(\pi \frac{\sigma_{s,k'} - \sigma_{u,k}}{N\Delta\sigma_u})}, \quad k = 0, N-1; k' = 0, N-1$
Big N, (N_0): Number of bins before decimation	$F[k,k'] = \frac{\Delta\sigma_s}{\Delta\sigma_u} \frac{Sin(\pi \frac{\sigma_{s,k'} - \sigma_{u,k}}{\Delta\sigma_u})}{N_0 Sin(\pi \frac{\sigma_{s,k'} - \sigma_{u,k}}{N_0\Delta\sigma_u})}, \quad k = 0, N-1; k' = 0, N-1$

The components in the CMO in different approaches can be in different orders and different forms. The resampling matrix (F) is a function which maps the raw spectra to the specified spectral grids and resolution. The two resampling matrix forms for different spectral bins are given in Table 1. $\Delta\sigma_s$ and $\Delta\sigma_u$ are the spectral resolution on sensor grid and user grid respectively. N_0 is the original digitized measured interferogram bin size, where N is the bin size after decimation. Decimation is part of a CrIS filtering process to reduce the data point in which a complex Finite Impulse Response (FIR) digital band-pass filter is used to reject the out-band signals and its image pass band. After this process, the original interferogram is decimated with a decimation factor DF to reduce the number bins from N_0 to N.

TABLE 2
DIFFERENT SELF-APODIZATION MATRIX FORMS

Self-apodization matrix (SA)	Expansion factor β; Bin size N
$SA[k',k] = \int_{\sigma_{\min}}^{\sigma_{\max}} \mathrm{Psinc}(\frac{\sigma_{k'} - \sigma'}{\Delta\sigma_u}, N) ILS(\sigma', \sigma_k) d\sigma'$, $k = 0, N-1, k' = 0, N-1$	β=1.0 for all three bands; small N
$SA[k',k] = \int_{\sigma_{\min}}^{\sigma_{\max}} \mathrm{Psinc}(\frac{\sigma_{k'} - \sigma'}{\Delta\sigma_u}, N_0) ILS(\sigma', \sigma_k) d\sigma'$, $k = 0, \beta N-1, k' = 0, \beta N-1$	β=1.4 (LW), 1.6 (MW) and 2.0 (SW), respectively; big N (N_0)

The self-apodization matrix (SA) can also be in different forms. Table 2 lists two SA matrixes using in this study. ILS is the instrument line shape function, and psinc is periodic sinc function.

The first calibration algorithm, referred as A1 [1], performing radiometric calibration first then spectral calibration, is the same as IDPS NSR system although some of the component algorithms differ:

$$S_{Cal} = SA^{-1} \cdot F \cdot f_{ATBD} \cdot \{\frac{S_e - < S_{SP} >}{< S_{ICT} > - < S_{SP} >} B_{ICT}\} \tag{1}$$

where S_{ICT}, S_{SP}, S_e are the raw spectra of the ICT, DS and Earth scene, respectively. The quantities inside of the angled brackets < > are averaged ICT or DS raw spectra within the moving window (30 consecutive spectra). S_{Cal}, B_{ICT}, and SA^{-1} are the calibration Earth spectra, the ICT radiance, and self-apodization correction matrix, respectively. SA and F are computed with large N (N_0) instead of small N as in the IDPS NSR system.

The second calibration algorithm, referred as A2, is based on [6] with SA and F computed with small N, the interferograms centered by adding phase to the raw spectra, and spectral correction performed first and then radiometric calibration:

$$S_{Cal} = B_{ICT} \frac{F \cdot f_{ATBD} \cdot SA^{-1} \cdot f_{ATBD} \cdot FIR^{-1} \cdot (S_e - < S_{SP} >)}{F \cdot f_{ATBD} \cdot SA^{-1} \cdot f_{ATBD} \cdot FIR^{-1} \cdot (< S_{ICT} > - < S_{SP} >)}. \tag{2}$$

The third calibration algorithm, referred as A3, is the same as A2, except SA and F are computed with large N (N_0) instead of small N as in A2.

The last calibration algorithm, referred as A4, is based on [7] with instrument phase dispersions to be removed before performing spectral correction:

$$S_{Cal} = B_{ICT} \frac{F \cdot f_{ATBD} \cdot SA^{-1} \cdot f_{ATBD} \cdot \{\frac{\Delta S_1}{\Delta S_2} |\Delta S_2|\}}{F \cdot f_{ATBD} \cdot SA^{-1} \cdot f_{ATBD} \cdot |\Delta S_2|}, \tag{3}$$

where

$$\Delta S_1 = FIR^{-1}(S_e - < S_{SP} >)$$

$$\Delta S_2 = FIR^{-1}(< S_{ICT} > - < S_{SP} >)$$

In A4, both SA and F are computed with large N (N_0).

3. SDR RADIANCE COMPARISON

We randomly selected 3 days FSR RDRs from 17 to 19 February 2015 to generated FSR SDRs using the four calibration algorithms in CRPS. The direct radiance comparisons were performed among these four algorithms using all data over night time. The data were averaged for nadir FORs (15th and 16th) independently for each FOV, and then compared forward and reverse sweep direction brightness (BT) differences and the mean BT differences from different algorithms.

The forward and reverse CrIS Earth spectra are separately calibrated using forward and reverse ICT and DS. Therefore, it is very important for the calibrated Earth spectra independent of the sweep directions. Fig. 1 shows the ringing artifact between forward sweep and reverse sweep at LWIR band for all corner FOVs (1, 3, 7, and 9) and FOV 5 (center FOV) from 648.75 cm^{-1} to 680 cm^{-1}. Larger ringing artifacts are shown in Algorithms 1 and 2 at the beginning edge of LWIR band. For Algorithm 1, the largest ranging happened at FOV 5, where Algorithm 2 has consistent large ringing for all FOVs. Algorithm 3 and 4 significantly reduce the sweep direction differences for all corner FOVs and side FOVs (not shown here), and the ringing at FOV 5 is the smallest. It indicates that Algorithms 3 and 4 are better approaches than Algorithms 1 and 2 in terms of sweep direction independence.

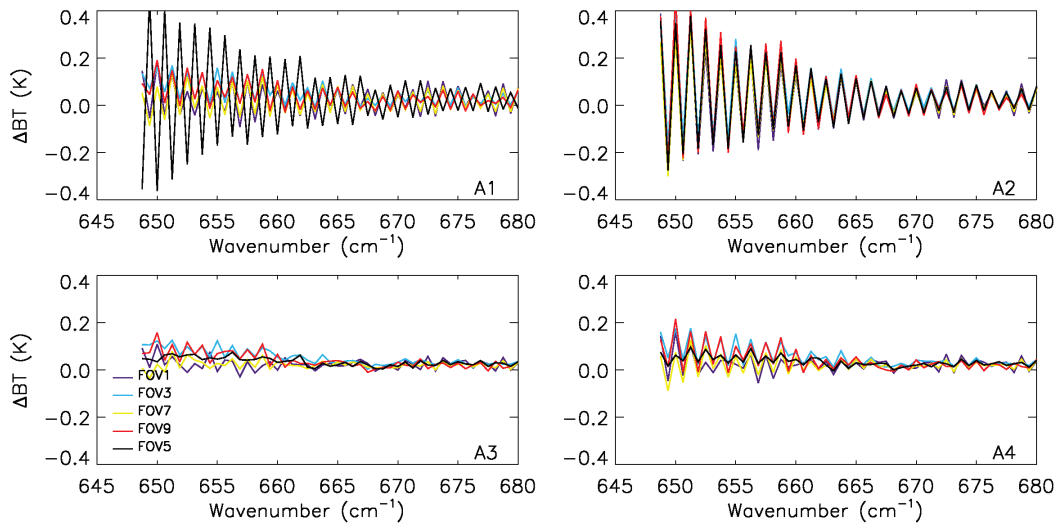

Fig. 1. Sweep direction BT differences (forward sweep BT at FOR 15 minus reverse sweep BT at FOR 16) for all four algorithms at corner FOVs and center FOV 5. The radiance spectra are unapodized.

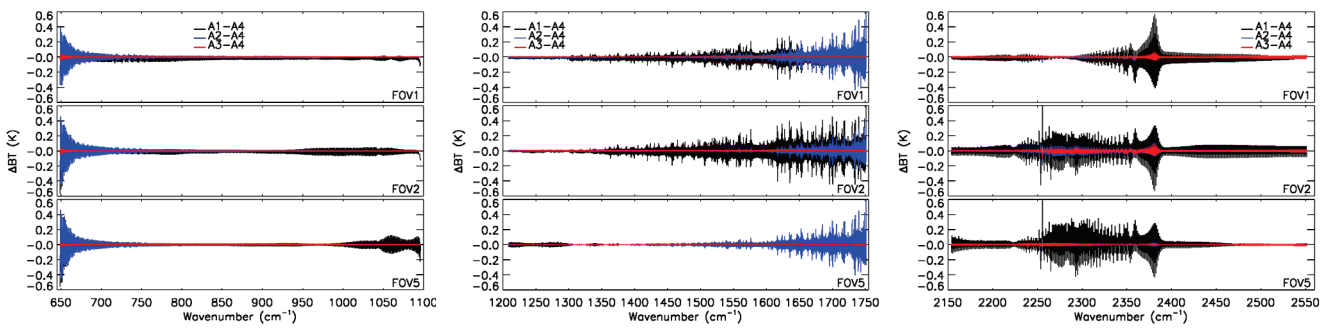

Fig. 2. Mean brightness temperature differences between other algorithms (1, 2, and 3) and algorithm 4 for LWIR (left panel), MWIR (middle panel), and SWIR (right panel) at FOVs 1, 2, and 5. The radiance spectra are unapodized.

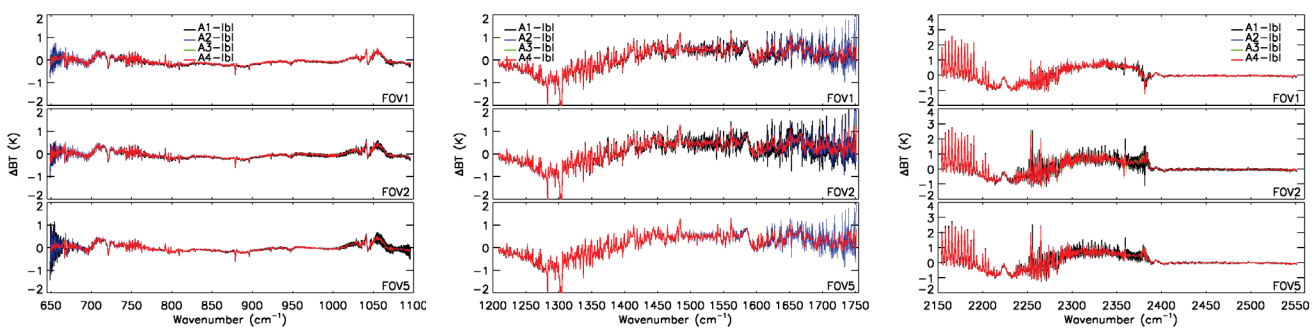

Fig. 3. Mean brightness temperature differences between observations in SDR from the four algorithms and Line-by-Line simulation over clear ocean scenes. The radiance spectra are unapodized.

Fig. 2 shows the mean BT difference between Algorithm 4 and other three algorithms. The comparison results show: For LWIR, Algorithm 1 has larger difference at the both band edges; Algorithm 2 only has large difference at the beginning of the band edge. For MWIR, Algorithms 1 and 2 have larger differences towards the end of band. For SWIR, Algorithms 1 has larger differences at the coldest lines and regions. For all bands, Algorithm 3 is basically the same as Algorithm 4.

4. EVALUATION OF DIFFERENT APPROACHES WITH LINE-BY-LINE SIMULATION

We developed the CrIS FSR SDR Validation System to quantify the CrIS radiometric and spectral accuracy [9], since they are crucial for improving its data assimilation in the numerical weather prediction, and for retrieving atmospheric trace gases. In this study, CrIS full resolution SDRs generated from CRPS using the four calibration approaches are assessed (in terms of absolute calibration bias, sweep direction difference, and FOV-2-FOV comparison) by using LBLRTM [10] v12.2 with spatially and temporally matched European Centre for Medium-Range Weather Forecasts (ECMWF) forecast fields as inputs. We first found night time clear ocean scenes for all 9 FOVs at nadir FORs (15th and 16th) over the above three day SDRs data. We also found all clear scenes at both FORs 15 and 16 at the same scan from these data, then simulated them using LBLRTM with spacing resolution at 0.001 cm^{-1} and default CH_4 and CO profiles.

The absolute calibration bias using LBLRTM simulation can be express as $BT_{obs} - BT_{lbl}$; the results are shown in Fig. 3. For LWIR, Algorithm 1 has larger difference at the both band edges; Algorithm 2 only has large difference at the beginning of the band edge; and Algorithm 3 and 4 have similar and best results compared to LBL simulation. For MWIR, Algorithms 1 and 2 have larger differences towards the end of band 2; and Algorithm 3 and 4 have similar and best results compared to LBL simulation. For SWIR, Algorithm 1 has larger differences at the coldest lines and regions; and Algorithms 2, 3 and 4 have similar and best results compared to LBL simulation.

The sweep direction differences (ringing) $(BT_{obs} - BT_{lbl})_{fwd} - (BT_{obs} - BT_{lbl})_{rev}$ (scene dependence is mostly removed by minus the LBL simulations) are almost the same as the results shown in Fig. 1 (not shown here).

The FOV-2-FOV consistence is an indication of variation among FOVs relative to center FOV 5: $(BT_{obs} - BT_{lbl})_{fov_i} - (BT_{obs} - BT_{lbl})_{fov_5}$. The MWIR results are shown in Fig. 4. Algorithms 2, and 4 are in very good agreement at the beginning of this band, but variation increasing towards the end of this band; Algorithm 1 shows larger variation than the other algorithms.

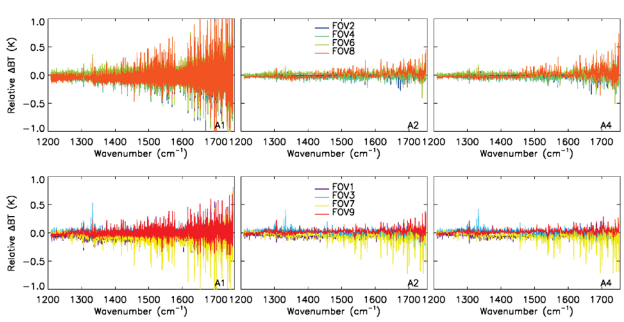

Fig. 4. FOV-2-FOV comparison relative to FOV 5 at MWIR for algorithms 1 (left panel), 2 (middle panel), and 4 (right panel). The radiance spectra are unapodized.

5. CONCLUSIONS

In this study, we have implemented four different calibration approaches in the CrIS full resolution SDR code in order to study the ringing effect observed in CrIS unapodized spectra and to support to select the best calibration algorithm for J1. Results show Algorithms 3 and 4 are the best choice in term of absolute bias, sweep direction difference (ringing artifact) reduction, and FOV-2-FOV consistence. Based on these results, we strongly recommend that Algorithm 4 as the J1 calibration algorithm to implement into J1 CrIS code since Algorithm 4 is more computationally efficient than Algorithm 3.

6. REFERENCES

[1] Y. Han, Y. Chen, X. Xiong, and X. Jin, "S-NPP CrIS full spectral resolution SDR processing and data quality assessment", the 95th AMS Annual Meeting, January 4-8, 2015, Phoenix, AZ, 2015.

[2] Y. Han, and Coauthors, "Suomi-NPP CrIS measurements, sensor data record algorithm, calibration and validation activities, and record data quality", J. Geophys. Res. Atmos., 118, doi:10.1002/2013JD020344, 2013.

[3] D. Tobin, and Coauthors, "Suomi-NPP CrIS radiometric calibration uncertainty", J. Geophys. Res. Atmos., 118, doi:10.1002/jgrd.50809, 2013.

[4] L. L. Strow, and Coauthors, "Spectral calibration and validation of the Cross-track infrared Sounder (CrIS) on the Suomi NPP satellite", J. Geophys. Res. Atmos., 118, doi:10.1002/2013JD020480, 2013.

[5] H. Revercomb, and Coauthors, "CrIS ringing artifacts: progress on implementing a correction", Weekly CrIS Calibration/Validation Teleconference, 24 September, 2014.

[6] D. Mooney, "CrIS Calibration Equation," STAR JPSS Annual Science Team Meeting, May 12-16, 2014, College Park, MD, 2014.

[7] J. Predina, Y. Han, D. Mooney, S. Atre, and L. Suwinski, "Future JPSS Cross-track Infrared Sounder (CrIS) ground algorithm improvements", OSA Hyperspectral Imaging and Sounding of the Environment (HISE) Conference, March 2-4, 2015, Lake Arrowhead, CA, 2015.

[8] Y. Chen, and Coauthors, "Comparison of different calibration approaches in S-NPP CrIS full spectral resolution processing", the 95th AMS Annual Meeting, January 4-8, 2015, Phoenix, AZ, 2015.

[9] Y. Chen, and Coauthors, "S-NPP CrIS full resolution sensor record processing and evaluations", 2014 AGU Fall Meeting, December 15-19, 2014, San Francisco, CA, 2014.

[10] S. A. Clough, and Coauthors, "Atmospheric radiative transfer modeling: a summary of the AER codes", Journal of Quantitative Spectroscopy and Radiative Transfer, 91, 233-244, doi:10.1016/j.jqsrt.2004.05.058, 2005.